



# Thermal Oxidative Degradation of Pure $\text{Cu}_2\text{S}$ and Industrial White Metal

M. Vázquez Vázquez<sup>1,2</sup> · M. J. Díaz Blanco<sup>3,4</sup> · R. A. Parra Figueroa<sup>5</sup> ·  
E. R. Balladares Varela<sup>5</sup> · O. Jerez Riveros<sup>6</sup> · M. Cuevas Cerda<sup>5</sup> ·  
I. Moreno-Ventas Bravo<sup>1,7</sup>

Received: 15 June 2023 / Revised: 5 July 2023 / Accepted: 5 July 2023 /  
Published online: 28 July 2023  
© The Author(s) 2023

## Abstract

The kinetics of the thermal oxidation of white metal and  $\text{Cu}_2\text{S}$  have been studied by thermogravimetric analysis (TG), which was carried out under atmospheric oxidative conditions ( $\text{O}_2$  100%) with heating rates of 5, 10, 15 and 20 °C  $\text{min}^{-1}$ . Each experiment was performed three times, the indicated values being the average of the three experiments. The experimental data were evaluated using isoconversional models based on the Arrhenius equation. The models are constructed using first-order mechanisms in the reactions and therefore, since most of them present adequate regression coefficients, it can be verified that order 1 is the most predominant order among the reactions found. In addition, the Kissinger–Akahira–Sunose model, which has the highest regression coefficient, is considered to be the most optimal. Similar behavior was recorded between  $\text{Cu}_2\text{S}$  and white metal, as well as a similar regular increase in the apparent activation energy ( $E_a$ ) of 10–30  $\text{kJ mol}^{-1}$  for both materials. The reactions that took place during the oxidation of white metal and  $\text{Cu}_2\text{S}$  were determined using a computational model based on thermodynamics developed in this work. The identified phases include  $\text{CuSO}_4$ ,  $\text{Cu}_2\text{SO}_4$ ,  $\text{Cu}_2\text{O}$ ,  $\text{CuO}$ ,  $\text{CuO}\cdot\text{CuSO}_4$ .

**Keywords** FactSage · Thermogravimetric analysis (TG) · Kinetic · White metal ·  $\text{Cu}_2\text{S}$  · Copper metallurgy

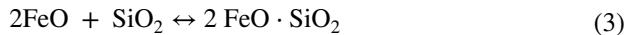
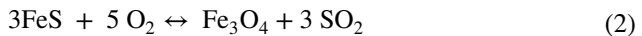
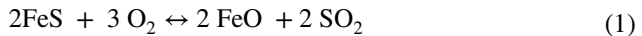
## Introduction

Copper is mainly obtained by industrial extraction processes involving copper sulfide ores. The two main industrial processes extraction types are pyrometallurgy (82% and hydrometallurgy (18%). Hydrometallurgy extracts copper from rich copper oxide ores in three stages: leaching, solvent extraction and electrowinning [1].

Pyrometallurgy is based on flash smelting, and the principal raw material used is a blend of copper concentrate, flux and reverts. The blend is mixed in the flash furnace with enriched air (oxygen-enriched air is working air with an oxygen percentage higher than 21 vol%) for smelting to obtain two immiscible liquids, matte and slag [2].

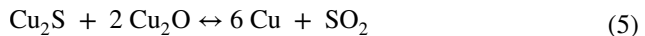
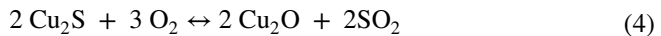
The oxygen-enriched phase compounds the molten slag, while the sulfide phases compound the molten matte. Copper sulfide is the main component in matte (50–70 wt.% Cu), with a minor amount of iron remaining as iron sulfide (5–20 wt.% Fe). The gas phase develops during the flash smelting process and is mainly composed of nitrogen and SO<sub>2</sub>. The molten phases, matte and slag, are separated by settling, and are mechanically transferred to processes in which liquid slag is usually processed in an electric furnace to recover copper losses in the slag, while liquid matte is refined into blister copper (99–99.5 wt.% Cu) in a copper converter furnace [3].

Copper conversion is a batch process consisting of two stages [4]. The first stage, slag making, separates the iron-rich phase from a mix of matte, flux and oxygen-enriched air. The matte is oxidized by enriched air added to the bath via tuyeres to obtain two immiscible phases, white metal mainly in the form of Cu<sub>2</sub>S (75–80 wt.% of Cu), and slag, mainly FeO. In general, the slag production process follows the reactions (Eq. 1–3).



Cu<sub>2</sub>S is the chief component of white metal, but it also contains other dissolved elements such as iron, precious metals and minor elements present in copper concentrates. The slag formed is mechanically removed from inside the converter furnace in order to continue with the copper production stage [5].

In the second stage of the conversion process, called copper making, the main objective is the oxidation of the white metal by oxygen-enriched air to form blister copper (99–99.5 wt.% Cu). During copper making, the reactions described by Eqs. 4 and 5 take place [1].



The reactions that occur in the copper-making stage are highly exothermic and, therefore, the copper-making process is autothermic. For this reason, scrap or cold copper-rich recycled material (cold charge) is added to maintain a working temperature of around 1250 °C [6].

The kinetic study in this work describes the conversion process of the oxidation kinetics that take place during the copper-making stage. To obtain this objective, we have used the oxidative degradation of materials is understood as the set

of reactions that the starting material, inside the crucible, undergoes due to the combined effect of thermal heating and reaction with oxygen. The raw materials used in the experiments in this study were industrial white metal and pure  $\text{Cu}_2\text{S}$ . Pure  $\text{Cu}_2\text{S}$  was selected because it is similar to industrial white metal, with a simpler composition than industrial materials.

This work studies the kinetic of the copper-making reactions in the conversion stage of the extractive copper industry. To this end, we have used the oxidative degradation of materials understood as the set of reactions that the starting material undergoes, inside the crucible, due to the combined effect of thermal heating and the reaction with oxygen.

Industrial control parameters, such as temperature, oxygen air enrichment, the amount of working gas or time required for the oxidation process, all need close control throughout the conversion process. These parameters are crucial in the copper smelting industry for minimizing costs, by adjusting working times and using the optimum quantity of working gas (oxygen efficiency) [7]. For this purpose, a study of the evolution of the reaction kinetics of the oxidation process of white metal and  $\text{Cu}_2\text{S}$  was carried out. The  $\text{Cu}_2\text{S}$  and white metal oxidation performed in this work aimed to resemble the copper-blowing stage in a copper conversion process. Several kinetic methods have been evaluated and the most suitable applied to this study.

In this work, we also studied the reactions that took place during the oxidation of  $\text{Cu}_2\text{S}$  with pure  $\text{O}_2$  based on a computational thermodynamic model. Although several published works have described some of the reactions that occur during  $\text{Cu}_2\text{S}$  oxidation [8–13], this present research has studied all the oxidation reactions of  $\text{Cu}_2\text{S}$  and their working temperatures, theoretically calculated by an innovative computational model that matches the results to the actual mass loss/gain obtained by the experimental thermogravimetry test.

## Experimental Procedures

### Materials

The raw materials for the experiments carried out were of two sources. A sample of pure copper sulfide supplied by Fisher Scientific, with a formula mass of  $159.14 \text{ g mol}^{-1}$ , density of  $5.6 \text{ g ml}^{-1}$  and purity of 99.5%.

The other sample was industrial white metal obtained by the oxidation of an industrial matte provided by Caletones Smelter (Codelco, Chile). The initial matte was oxidized by adding a silicate flux in order to yield the slag phase of the fayalitic type. The slag produced is easily removed because it remains as liquid on the surface, since it has lower density than white metal. The remaining white metal was used as one of the raw materials in this study (Fig. 1).

A typical white metal composition from a pyrometallurgical smelter is shown in Table 1. These white metal range values concur with the white metal composition studied in the present work.

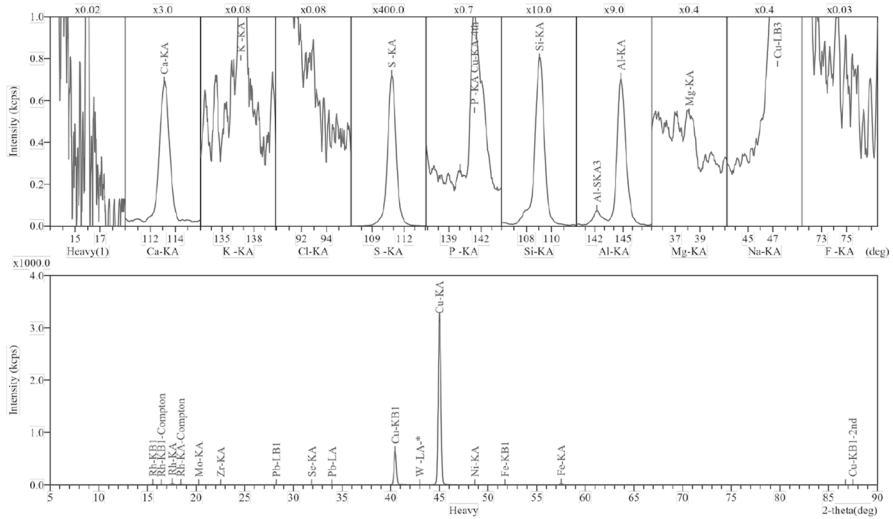


**Fig. 1** White metal X-ray diffraction; Ca: Calcium; K: Potassium; Cl: Chlorine; S: Sulfur; P: Phosphorus; Si: Silicon; Al: Aluminum; Mg: Magnesium; Na: Sodium; F: Fluorine; Mo: Molybdenum; Zr: Zirconium; Pb: Lead; Se: Selenium; Cu: Copper; W: Tungsten; Ni: Nickel; Fe: Iron

**Table 1** Compositional analysis of typical white metal in mass %

Element	Mass	Element	Mass
Cu	76.70 ± 4.71	Pb	0.16 ± 0.05
S	17.69 ± 1.86	Mg	0.04 ± 0.07
Si	1.83 ± 1.70	Se	0.03 ± 0.01
Al	0.50 ± 0.25	Ni	0.11 ± 0.05
Fe	2.00 ± 1.67	P	0.16 ± 0.05
Ca	0.43 ± 1.53	K	<0.01 ± 0.01

**Table 2** Compositional analysis by X-ray fluorescence of white metal in percentage

Element	Mass	Detection limit	Element	Mass	Detection limit
Cu	82.76	0.01	Pb	0.08	0.011
S	14.56	0.02	Mg	0.03	0.023
Si	0.86	0.01	Se	0.03	0.005
Al	0.72	0.01	Ni	0.02	0.006
Fe	0.65	0.01	P	0.02	0.004
Ca	0.24	0.01	K	<0.01	0.004

The composition of the white metal used in this work was analyzed using the Rigaku ZSX primus II model X-ray fluorescence spectrometer. The results obtained by X-ray fluorescence are shown in Table 2.

The white metal used in this study was analyzed by X-ray diffraction with the Bruker D4 endeavor diffractometer, using copper radiation excited with a current of 20 mA and 40 kV voltage. The working conditions were a scan interval of  $3^\circ$  to  $70^\circ$  of  $2\theta$ , an increase in angle step of  $0.02^\circ$  and an exposure time per step of 1 s. The results obtained by X-ray diffraction confirmed that the composition of the white metal sample was  $\text{Cu}_2\text{S}$  by more than 97%. Figure 2 is the diffractogram obtained for the white metal sample. The top of the Fig. 2 represents the enlargement for the peaks detected in the XRD represented in the bottom of the Fig. 2.

FRX and DRX analyses concur in sample impurities content (copper and sulfur exceeded 97%).

The pure copper sulfide with ground to a mesh powder of less than 200 microns was acquired. The white metal was ground in a Fritsch Pulverisette ball mill for five minutes at 450 r.p.m., which yielded material of less than 200 microns.

### Differential Optical Absorption Spectroscopy (DOAS)

A DOAS analyzer (Unisearch Associates Inc.) was used to measure the composition of the gas produced. The DOAS analyzer determines the concentration of  $\text{SO}_2$  in volume percentage by comparing the absorption signals to their stored reference signals. The DOAS analyzer uses four simultaneous analysis channels, each applied to different concentration values, from ppm scale to high  $\text{SO}_2$  concentration.

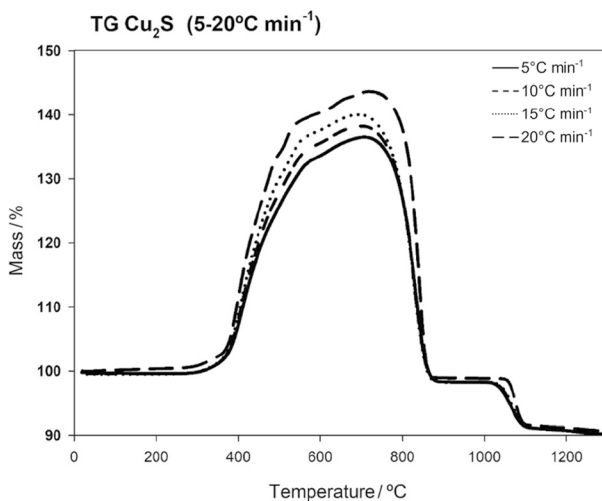


**Fig. 2** Mass loss profile thermograms for  $\text{Cu}_2\text{S}$  in relation to four heating rates. Continuous line:  $5^\circ\text{C min}^{-1}$ ; short-dashed line:  $10^\circ\text{C min}^{-1}$ ; dotted line:  $15^\circ\text{C min}^{-1}$ ; long dashed line:  $20^\circ\text{C min}^{-1}$ .

## Thermodynamic Calculation

The FactSage Equilib module was used in the thermodynamic calculation [14–17]. This software uses the Gibbs energy minimization model to calculate the association of equilibrium phases and their composition. Taking these results, calculated at short intervals of increasing temperature, a study was made of the reactions that occurred in this temperature range.

In this study, the aim of the model was to fit the thermodynamic calculation in order to reproduce the experimental thermogravimetric analysis (TG) curve. To achieve this required modulating the efficiency of the oxidative process.

To make the thermodynamic calculations model, it was necessary to know the starting conditions of the system studied, such as composition, temperature and phase state. The parameters adjusted to this study were the mass of the real system inside the crucible used in thermal analyzer, the increasing temperature of the system and the efficiency of the oxidation process. The oxidation efficiency was to reproduce the temperature mass pairs reported in the TG curve. In this study, we calculated the chemical equilibrium of each 0.1 °C difference to obtain all possible reactions that would take place during copper sulfide oxidation, from 25 to 1300 °C, until no further change in mass was observed in the TG analysis. In each calculation, we assumed that the initial composition of each system studied was the final composition of the previous system.

## Thermogravimetric Analysis Equipment

The kinetic behavior of  $\text{Cu}_2\text{S}$  was studied by thermogravimetric analysis (TG) [18]. Three parameters were registered in TG: the mass of the crucible that contains the  $\text{Cu}_2\text{S}$  sample, temperature of the crucible and time. TG methodology evolves the mass change of the crucible at the same time that the temperature steeply increases. The oxidant air flow is controlled specifically for the process. As a result a curve of mass versus time and temperature is obtained. In this study, a thermogravimetric analyzer (Simultaneous Thermal Analysis 449 F3 Jupiter, NETZSCH) to verify the thermochemical response of  $\text{Cu}_2\text{S}$  was used. The TG experiments were performed by heating a 50 mg sample from 25 to 1300 °C at heating rates of 5, 10, 15 and 20 °C  $\text{min}^{-1}$ , respectively, in an oxygen dynamic flow rate of 20  $\text{cm}^3 \text{min}^{-1}$ . The conditions used in the test are similar to those used in the work on kinetic of pyrite by Vázquez [19].

Each experiment was performed three times, with the values reported being the average of the three experiments. The averages obtained have a standard deviation below 10%.

## Kinetic Methods

Several isoconversional methods to evaluate the evolution of the kinetic parameters for the reactions that took place has been studied. The kinetic parameters

included the activation energy ( $E_a$ ), the pre-exponential factor ( $A$ ) and the reaction order ( $n$ ). In this respect, techniques such as thermogravimetry (TG) and derivative thermogravimetry (DTG) analyses are commonly employed to calculate the kinetic parameters of oxidation reactions [9–13, 20]. All these methods are based on the general Arrhenius equation (Eq. 6).

$$\frac{d(\alpha)}{dt} = k(T)f(\alpha) \tag{6}$$

In this form,  $d\alpha/dt$  is the reaction rate ( $\text{min}^{-1}$ ),  $\alpha$  is the fractional conversion,  $k(T)$  is the rate constant and  $f(\alpha)$  is a function of reaction degree.

The Arrhenius equation enables us to obtain Eq. 7.

$$\frac{d(\alpha)}{dt} = Ae^{\left(-\frac{E_a}{RT}\right)}f(\alpha) \tag{7}$$

where  $A$  is the pre-exponential factor ( $\text{min}^{-1}$ ),  $E_a$  is the apparent activation energy ( $\text{J mol}^{-1}$ ),  $T$  is the temperature (K) and  $R$  is the ideal gas constant ( $\text{J K}^{-1} \text{mol}^{-1}$ ) [21].

Equation 8 is obtained by integrating and rearranging the above equation.

$$g(\alpha) = \int_0^\alpha \frac{d(\alpha)}{f(\alpha)} = \frac{A}{\beta} \int_{T_0}^T e^{\left(-\frac{E_a}{RT}\right)} dT \tag{8}$$

where  $g(\alpha)$  is the integral form of  $f(\alpha)$ ,  $\beta$  is the heating rate ( $\text{K min}^{-1}$ ),  $T_0$  is the initial temperature (K) and  $T$  is the final temperature (K) of the non-isothermal experiment.

It is clear that  $g(\alpha)$  implies a general function that will depend on each particular reaction. In general, the reaction function  $g(\alpha)$  could also involve more than one reaction, in other words, multiple reactions occurring at the same temperature, each of which has its specific degree of conversion, thus involving the general function of the conversion rate of the total system that cannot be calculated exactly. Therefore, different approximations to express  $g(\alpha)$  have been applied in this study [22–28]. Some of the approximations used in this research are described in Table 3.

Netzsch Kinetics Neo software (v2.1.2.1) was used to determine  $E_a$  and the pre-exponential factor ( $A$ ) using the methods described above.

**Table 3** Methods to calculate kinetic degradation parameters using TG data

Method	Mathematical expression*	Reference
Friedman	$\ln\left(\frac{d\alpha}{dt}\right) = \ln(Af(\alpha)) - \frac{E_a}{RT}$ (9)	[22]
Coats—Redfern	$\ln\frac{g(\alpha)}{T^2} = \ln\frac{AR}{\beta E} \left(1 - \frac{2RT}{E_a}\right) - \frac{E_a}{RT}$ (10)	[23, 24];
Kissinger—Akahira—Sunose (KAS)	$\ln\left(\frac{\beta}{T^2}\right) = \ln\left(\frac{AR}{g(\alpha)E_a}\right) - \frac{E_a}{RT}$ (11)	[25, 26]
Flynn—Wall—Ozawa (FWO)	$\log(\beta) = \log\left[\frac{AE_a}{g(\alpha)R}\right] - 2.315 - \frac{0.457E_a}{RT}$ (12)	[27, 28]

\*Different selected functions for  $f(\alpha)$  and  $g(\alpha)$  according to the model selected and reaction order

## Results and Discussion

### Chemical Analysis

The identification, quantification and control of components other than  $\text{Cu}_2\text{S}$  in white metal could be, a priori, a relevant aspect in determining correct process development, particularly because of problems that could arise due to possible reactions or collateral physical phenomena.

Table 2 presents the white metal's chemical composition, with the copper sulfide sample at 99.5wt.% ( $\text{Cu}_2\text{S}$ ) and appreciable amounts of Si (0.86%), Al (0.72%) and Fe (0.65%).

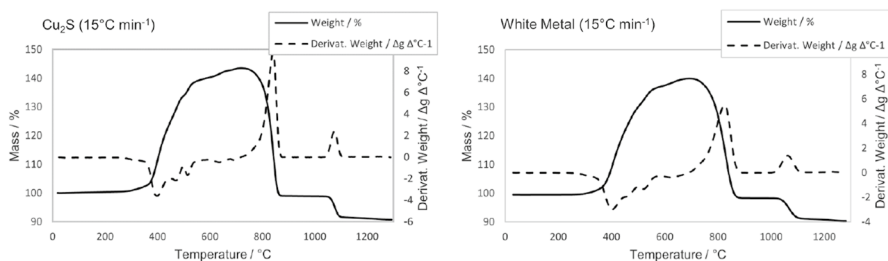
### Comparative Evolution of Results Obtained in the Thermogravimetric Analysis of Pure $\text{Cu}_2\text{S}$ and Industrial White Metal

Figure 2 shows the evolution of the TG curves for  $\text{Cu}_2\text{S}$  at four heating rates under oxidizing conditions. As expected, changes in the curves were observed when examining the various heating rates of the same material, due to the kinetic nature of the TG events. In this regard, higher heating rates result in a lower resolution of the curve since the reactions occur faster. On the other hand, lower heating rates take longer to produce such reactions, and greater sensitivity may result.

The curves made with 5, 10, 15 and 20  $^\circ\text{C min}^{-1}$  have a great geometrical similarity in the trends shown by the set. For this reason, one of the curves has been selected to be shown in isolation and to explain its mass variation step by step. The selected curve represented in Fig. 3 is the 15  $^\circ\text{C min}^{-1}$  curve because it is a curve made at an intermediate heating ramp.

Figure 3 presents the thermograms corresponding to the mass loss profile (TG) and its derivative curve (DTG) for  $\text{Cu}_2\text{S}$  and white metal, with respect to the temperature for its oxidative decomposition at 15  $^\circ\text{C min}^{-1}$ . Four thermograms were made to calculate the kinetic parameters, but only the thermogram corresponding to 15  $^\circ\text{C min}^{-1}$  is presented here to show the evolution of the thermal oxidation.

The mass versus temperature continuous curves displayed in Fig. 3 for pure  $\text{Cu}_2\text{S}$ , and white metal exhibits remarkable similarity. Moreover, the derivative mass



**Fig. 3** TG and DTG corresponding to the oxidative decomposition of  $\text{Cu}_2\text{S}$  and white metal at 15  $^\circ\text{C min}^{-1}$



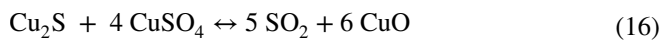
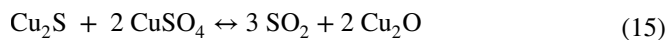
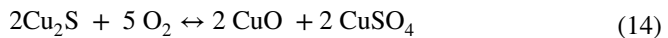
curves (represented by the discontinuous trace) demonstrate analogous behavior, with the peaks of the discontinuous curves coinciding in both cases. This observation strongly suggests that both pure  $\text{Cu}_2\text{S}$  and white metal undergo identical reactions during the heating process, supporting the aforementioned conclusion [8–10].

In Fig. 3, the TG curve indicates an absence of mass loss or mass gain (absence of chemical reaction) up to 250 °C. Above that temperature, a similar profile of the two samples emerges, and different phases, according to temperature, can be observed.

The TG curve in the range 250–570 °C shows a mass increase of 39% for  $\text{Cu}_2\text{S}$  and 27% for white metal, which could be related to the greater abundance of  $\text{Cu}_2\text{S}$  in the “pure  $\text{Cu}_2\text{S}$  sample” than in the white metal sample. The process in this range is related to copper sulfide oxidation to form copper sulfate, as confirmed by TG and DTG peaks. This mass increase due to the formation of sulfates, in accordance with Dunn [12], can be associated to the following reaction (Eq. 13).

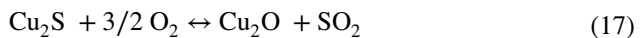


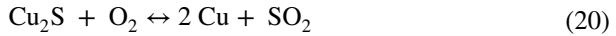
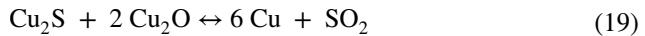
However, Burger [11] reported that different reactions can occur in parallel giving rise to the general reaction described by Eq. 13. In this sense, these studies show that, in temperatures below 500 °C, the main reaction corresponds to that presented in Eq. 14, and for temperatures between 500 and 700 °C, to Eq. 15 and Eq. 16.



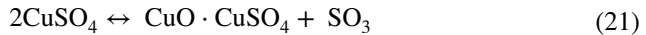
Following this previous step, the TG curves (Fig. 3) show a shallower slope in the range of 570–720 °C, approximately. From the data provided by Wang et al. [9] and Zuo et al. [10],  $\text{Cu}_2\text{O}$  oxidizes to  $\text{CuO}$  above 260 °C and transforms to  $\text{CuO}$  under higher temperatures. Furthermore, above 400 °C, S oxidation and a continuous degradation of  $\text{Cu}_2\text{S}$  occurs, resulting in different  $\text{Cu}_x\text{O}$  compounds being formed, although compounds with  $x=2$  are the most frequently reported. This mass gain by the oxidation of copper sulfides to form copper sulfate and oxysulfate is confirmed by TG and DTG peaks (at 550 and 720–760 °C). Nafees et al. [13] described the formation of copper sulfates from copper sulfide at temperatures described in the same range.

In the 720–870 °C range, the TG curves (Fig. 3) show a pronounced mass loss related to the oxidation of sulfur to sulfur dioxide. At this stage, as a result of the elimination of the sulfur content as  $\text{SO}_2$ , a significant mass decrease to contents similar to the initial ones at temperatures close to 870 °C takes place. Ramakrishna and Abraham [8] showed that, in the 750°–950 °C range, the oxidation of copper sulfides takes place according to Eq. 17–20.





Alternatively, according to Dunn and Muzenda [12], part of the CuO can be yielded above 900 °C, also due to the decomposition of sulfates generated in the previous phase (Eq. 21–22).



No significant alteration was observed between 870 and 1000 °C. The removal of sulfur compounds, reaching masses similar to the initial ones, was verified in this step.

In the 1000–1300 °C stage, the TG curves show a mass loss of around 9%. Li and Mayer [29] and Yi et al. [30] related this mass loss to the reaction in Eq. 23.



In this study, we modeled the TG curve around thermodynamic calculations to reproduce the crucible mass evolution using oxygen efficiency to control the mass gain/loss. New equations for each temperature range were generated with the model developed in this work (Sect. "Oxidation reactions of Cu<sub>2</sub>S"). Oxidation reactions of Cu<sub>2</sub>S).

### Oxidation Reactions of Cu<sub>2</sub>S

A computational thermodynamic method to determine the reactions involved in the Cu<sub>2</sub>S oxidation process in an oxidative environment has been developed. Through this method, the chemical equilibria were calculated at each point of the experimental TG curve. The computational method developed improves empirical methods for determining the phases formed during Cu<sub>2</sub>S oxidation because our method allows us to determine the oxidation state of elements in each phase formed.

By merging kinetic and thermodynamic models, the temperatures found for the different reactions following the FactSage Equilib module have been modulated to fit the changes found in the TGA profile.

The starting material used for thermodynamic calculation was the same as in the experimental TG. The working gas used in the thermodynamic calculation was restricted to ensure that the reaction advance equaled the experimental mass TG curve. The limited availability of the working gas was the method used to apply oxygen efficiency in order to reproduce the crucible mass in each calculation step. Table 4 shows the oxygen efficiency average data in each temperature range.

**Table 4** Reactions calculated according to the FactSage Equilib module applied to the different temperature ranges studied

Temperature ranges/°C	Oxygen efficiency/%	Reactions
250.0–353.6	0.23	$2 \text{Cu}_2\text{S} + 9/2 \text{O}_2 \leftrightarrow \text{Cu}_2\text{O} + 2 \text{CuSO}_4$ (24)
353.6–416.3	2.44	$\text{Cu}_2\text{S} + 2 \text{O}_2 \leftrightarrow \text{Cu}_2\text{SO}_4$ (25)
416.3–434.4	8.48	$4 \text{Cu}_2\text{S} + 7 \text{O}_2 \leftrightarrow 2 \text{Cu}_2\text{O} + 2 \text{Cu}_2\text{SO}_4 + \text{SO}_2$ (26)
434.4–490.8	4.61	$3 \text{Cu}_2\text{S} + 6 \text{O}_2 \leftrightarrow 2 \text{Cu}_2\text{O} + 2 \text{CuSO}_4 + \text{SO}_2$ (27)
490.8–573.7	1.80	$3 \text{Cu}_2\text{O} + \text{Cu}_2\text{S} + 6 \text{CuSO}_4 + 4 \text{O}_2 \leftrightarrow 7(\text{CuO} \cdot \text{CuSO}_4)$ (28)
573.7–718.5	1.40	$12 \text{Cu}_2\text{O} + 2/5 \text{Cu}_2\text{S} + 7 \text{O}_2 \leftrightarrow 24 \text{CuO} + 25(\text{CuO} \cdot \text{CuSO}_4)$ (29)
718.5–873.5	–	$(\text{CuO} \cdot \text{CuSO}_4) \leftrightarrow 2 \text{CuO} + 1/2 \text{O}_2 + \text{SO}_2$ (30)
1118.5–1228.5	–	$4 \text{CuO} \leftrightarrow 2 \text{Cu}_2\text{O} + \text{O}_2$ (31)

Eight different reactions were determined for  $\text{Cu}_2\text{S}$  oxidation. The experimental TG curve (continuous line) of the  $\text{Cu}_2\text{S}$  oxidation process and the thermodynamic curve calculated (dashed lines) are presented in Fig. 4. The starting temperature of each calculated reaction is shown by points on the TG curve Fig. 4.

The calculated reactions and oxygen efficiency are shown in Table 4.

The initial mass increase at 250 °C starts with the  $\text{Cu}_2\text{S}$  oxidation reaction (Eq. 24). It was determined that the initial mass increase in the  $\text{Cu}_2\text{S}$  oxidation related to the formation of  $\text{CuO}$  and  $\text{CuSO}_4$ . The reaction obtained in this work

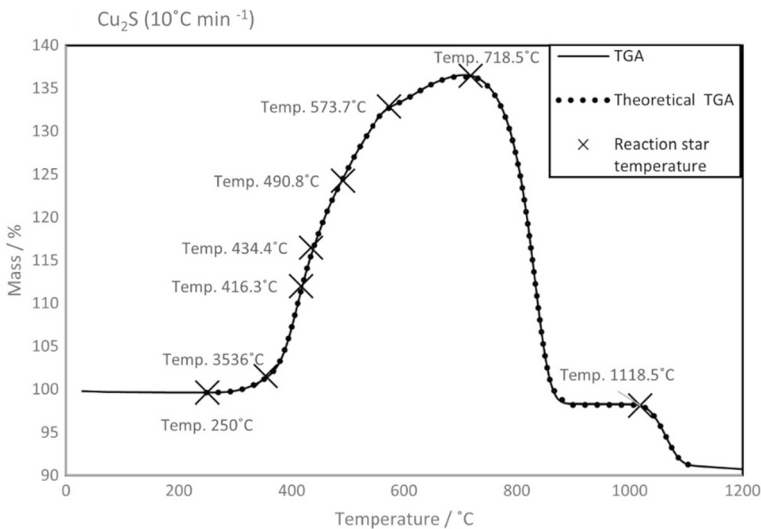


**Fig. 4** Comparative evolution of the experimental and estimated TG curves for  $\text{Cu}_2\text{S}$ , in  $10 \text{ }^\circ\text{C min}^{-1}$  heating rate

for the initial mass change matches Dunn and Muzenda [12], as does the sulfate formation associated to the mass increase, also described in this study.

In the 353.6–416.3 °C range, the starting material was 95.39%  $\text{Cu}_2\text{S}$ , 3.18%  $\text{CuSO}_4$ , 1.43%  $\text{Cu}_2\text{O}$ , as shown in Fig. 5. In the temperature range studied, the formation of  $\text{Cu}_2\text{SO}_4$  starts with  $\text{Cu}_2\text{S}$  oxidation (Eq. 25). The mass increase (10.5%) has an oxygen efficiency of 2.44% from the  $20 \text{ cm}^3 \text{ min}^{-1}$  added in the TG.

In the 416.3–490.8 °C temperature band, gaseous  $\text{SO}_2$  was formed as a result of  $\text{Cu}_2\text{S}$  oxidation. In this temperature range, two different reactions took place (Eq. 26–27). The output gas empirical measurement of the thermogravimetric test showed  $\text{SO}_2$  gas production at between 418 and 502 °C (Fig. 6).

Following the previous stage, two different reactions occurred in the 490.8–718.5 °C temperature range (Eq. 28–29). The compositional evolution of the crucible mass is shown in Fig. 5. The main phase formed in this temperature range was  $\text{CuO}\cdot\text{CuSO}_4$ . This phase was also described by Dunn and Muzenda [12] and Nafees et al. [13] for  $\text{Cu}_2\text{S}$  oxidation.

At 718.5 °C, all  $\text{Cu}_2\text{S}$  had been oxidized. The Eq. 30 reaction describes the mass loss in the slope curve from 718.5 to 873.5 °C where the final reaction product is  $\text{CuO}$  and  $\text{SO}_2$  gas. The same reaction was described by Nafees et al. [13] for the 630 °C–840 °C temperature range.

Sulfur dioxide production in the 624–863 °C range is shown in Fig. 6. The  $\text{SO}_2$  curve was obtained empirically by measuring the off-gas produced during the TG test. The temperature range at which  $\text{SO}_2$  was produced was consistent with the reaction (Eq. 30) obtained by the computational thermodynamic model.

The mechanism proposed through the sequence of reactions in Table 4 (modeled in Fig. 5) fully coincides, as far as  $\text{SO}_2$  evolution is concerned, with the DOAS measurements (Fig. 6).

The reaction described by Eq. 30 is a highly exothermic process. The exothermic process causes the real temperature inside the crucible to increase. The reaction described for the last mass loss (Eq. 31) starts at 1118.5 °C according to the

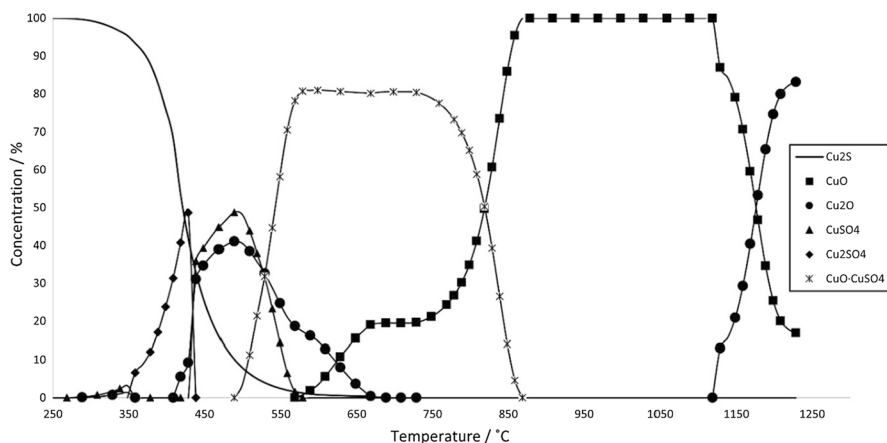


**Fig. 5** Phases in the evolution of  $\text{Cu}_2\text{S}$  oxidation concentration as a function of temperature

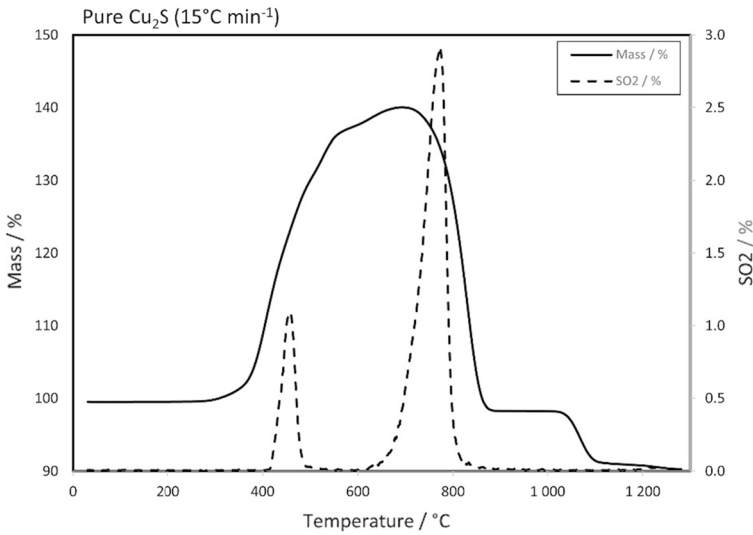


**Fig. 6** TG curve corresponding to the oxidative decomposition of  $\text{Cu}_2\text{S}$  at  $15\text{ }^\circ\text{C min}^{-1}$ ; the  $\text{SO}_2$  curve corresponds to the DOAS measurement

computational thermodynamic model developed in this work. There is a difference between the TG temperature and the reaction (Eq. 31) starting temperature calculated by the model. In this study, we have tried to explain this temperature decalage by means of a thermal difference between the temperature registered by the TG equipment at this stage and the real temperature within the crucible.

**Comparative Kinetic Evolution of  $\text{Cu}_2\text{S}$  and White Metal**

Table 5 shows that the Kissinger–Akahira–Sunose method seems to be the most suitable to represent (as a whole) the evolution of  $\text{Cu}_2\text{S}$  oxidation (pure and white metal). This may be due to the good applicability of this method to temperature programs other than linear heating [31–33] which, in this case, having both exothermic and endothermic reactions, is especially important. The regression

**Table 5** The results of the application of the different methods presented in Table 3

Method	$\text{Cu}_2\text{S}$		White metal	
	$R^2$	Df	$R^2$	df
Friedman	0.561	1.965	0.797	1.963
Coats–Redfern (1 <sup>st</sup> order)	0.896	1.965	0.935	1.963
Coats–Redfern (2 <sup>nd</sup> order)	0.751	1.965	0.910	1.963
<u>Kissinger–Akahira–Sunose</u>	<u>0.995</u>	<u>1.965</u>	<u>0.988</u>	<u>1.963</u>
Flynn–Wall–Ozawa	0.921	1.965	0.916	1.963

The underlined row corresponds to the most appropriate method among those studied

coefficient values obtained for the Coats-Redfern (1st order) model are also higher than those obtained for Coats-Redfern (2nd order). This supports the supposition that the first order is the dominant order of reaction, which is the one used in the Kissinger–Akahira–Sunose model. Experimentally, this method shows that the activation energy is determined by the slope of the graph of  $\ln\left(\frac{\beta}{T^2}\right)$  versus  $\frac{1000}{T}$  (Fig. 7).

Figure 7 shows the activation energy evolution for both starting materials studied, using the Kissinger–Akahira–Sunose method.

Similar behavior between  $\text{Cu}_2\text{S}$  and white metal was found, with similar  $E_a$  values that differs 1–3  $\text{kJ mol}^{-1}$  for both materials for a conversion variation of 0.1–0.9 corresponding to absolute  $E_a$  values in the range of 10–30  $\text{kJ mol}^{-1}$  (Fig. 7). It should be noted that the values calculated for  $\text{Cu}_2\text{S}$  were significantly lower throughout the entire conversion range than those found for white metal; the variation in the values calculated to the different quality of the raw material used must be taken into account. On the other hand, the values obtained were similar to those in Barrios García [5] (24  $\text{kJ mol}^{-1}$ ), Jalkanen [34] (10.5  $\text{kJ mol}^{-1}$ ) and Ramakrishna and Abraham [8] (25  $\text{kJ mol}^{-1}$ ).

## Conclusions

The evolution of the thermal oxidation of  $\text{Cu}_2\text{S}$  and white metal samples by thermogravimetric analysis has been studied. TG and DTG analyses showed similar behavior for  $\text{Cu}_2\text{S}$  and white metal.

Five phases, which corresponded to increases and decreases in sample mass, of the thermal oxidation of these samples were identified:  $\text{CuSO}_4$ ,  $\text{Cu}_2\text{SO}_4$ ,  $\text{Cu}_2\text{O}$ ,  $\text{CuO}$ ,  $\text{CuO}\cdot\text{CuSO}_4$ .

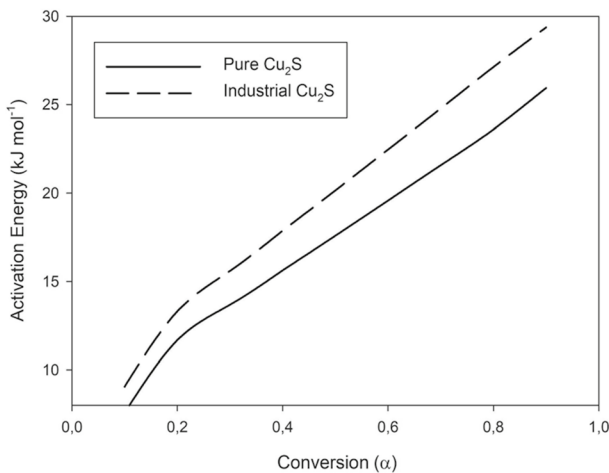


**Fig. 7** Activation energy evolution calculated by the Kissinger–Akahira–Sunose method for  $\text{Cu}_2\text{S}$  and white metal

Among the methods studied for kinetic data analysis, the Kissinger–Aka-hira–Sunose method seemed to be the most suitable.

Activation energy evolution with respect to the degree of conversion indicated lower values of this parameter for  $\text{Cu}_2\text{S}$  with respect to industrial white metal.

A non-empirical methodology based on computational thermodynamic calculations to reproduce the  $\text{Cu}_2\text{S}$  oxidation TG curve, by performing oxidative restriction in the process, has been developed, and a very accurate mass loss/gain match to the TG measurements was obtained.

The analysis of  $\text{SO}_2$  in the off-gas produced during  $\text{Cu}_2\text{S}$  oxidation was consistent with the reactions obtained by the non-empirical thermodynamic model developed.

**Acknowledgements** This work was carried out with financial support from the Research and Transfer Policy Strategy of the University of Huelva (Call for Industrial Doctorate grants at the University of Huelva), and from Atlantic Copper S.A.U. The authors also wish to thank the GEA Institute of the Universidad de Concepción, Chile, whose facilities were made available to us to carry out a significant part of the experimental work performed. Special thanks to Hugo Rojas, metallurgical engineer responsible for laboratory equipment used in this study.

**Author Contributions** All authors wrote the main manuscript text and reviewed the manuscript.

**Funding** Funding for open access publishing: Universidad de Huelva/CBUA.

## Declarations

**Conflict of interest** The author declare that they have no conflict of interest.

**Open Access** This article is licensed under a Creative Commons Attribution 4.0 International License, which permits use, sharing, adaptation, distribution and reproduction in any medium or format, as long as you give appropriate credit to the original author(s) and the source, provide a link to the Creative Commons licence, and indicate if changes were made. The images or other third party material in this article are included in the article's Creative Commons licence, unless indicated otherwise in a credit line to the material. If material is not included in the article's Creative Commons licence and your intended use is not permitted by statutory regulation or exceeds the permitted use, you will need to obtain permission directly from the copyright holder. To view a copy of this licence, visit <http://creativecommons.org/licenses/by/4.0/>.

## References

1. W. G. Davenport, M. J. King, M. E. Schlesinger, and A. K. Biswas, *Extractive metallurgy of copper*. Elsevier. 2002. <https://doi.org/10.1016/C2010-0-64841-3>.
2. M. Laputka and W. Xie, *Mining, Metallurgy and Exploration* **38**, 2021 (1135–1165). <https://doi.org/10.1007/s42461-021-00386-y>.
3. J. P. Sancho, L. F. Verdeja, A. Ballester, *Metalurgia Extractiva*. Volumen II: Procesos de obtención. Madrid: Edited by Sintesis. 2000. ISBN 84–7738–803–2.
4. N. Cardona, P. J. Mackey, P. Coursol, R. Parada, and R. Parra, *JOM*. **64**, (5), 2012 (546–550).
5. P. Barrios García, *Cinética en la etapa de conversión para la obtención pirometalúrgica del cobre*. (Tesis Doctoral Inédita). Universidad de Sevilla, Sevilla. 2004
6. I. Pérez, I. Moreno-Ventas, G. Ríos, and T. Bravo, *Metallurgical and Materials Transactions B* **51**, 2020 (1432–1445). <https://doi.org/10.1007/s11663-020-01844-6>.
7. B. Zhao and J. Liao, *Metals*. **12**, (2), 2022 (190). <https://doi.org/10.3390/met12020190>.
8. V. Ramakrishna Rao and K. P. Abraham, *Metallurgical Transactions*. **2**, (9), 1971 (2463–2470).

9. X. Wang, Z. Huang, M. Wei, T. Lu, D. Nong, J. Zhao, X. Gao, and L. Teng, *Thermochimica Acta*. **672**, 2019 (14–24). <https://doi.org/10.1016/j.tca.2018.12.008>.
10. Y. Zuo, Y. Liu, J. Li, R. Du, X. Han, T. Zhang, J. Arbiol, N. J. Divins, J. Llorca, N. Guijarro, K. Sivula, and A. Cabot, *Chemistry of Materials*. **31**, (18), 2019 (7732–7743). <https://doi.org/10.1021/acs.chemmater.9b02790>.
11. E. Burger, D. Bourgarit, V. Frotté, and F. Pilon, *Journal of thermal analysis and calorimetry*. **103**, (1), 2011 (249–256).
12. J. G. Dunn and C. Muzenda, *Journal of thermal analysis and calorimetry*. **64**, (3), 2001 (1241–1246). <https://doi.org/10.1023/A:1011513616930>.
13. M. Nafees, M. Ikram, and S. Ali, *Digest Journal of Nanomaterials and Biostructures*. **10**, (2), 2015 (635–641).
14. C. W. Bale, P. Chartrand, S. A. Degterov, G. Eriksson, and K. Hack, *FactSage thermochemical software and databases*. *Calphad*. **26**, (2), 2002 (189–228).
15. C.W. Bale, E. Bélisle, P. Chartrand, S.A. Deckerov, G. Eriksson, S. Hack & Petersen FactSage thermochemical software and databases—recent developments. *Calphad*. 2009; 33(2); 295–311.
16. C. Bale, E. Bélisle, P. Chartrand, S. Deckerov, G. Eriksson, A. Gheribi, K. Hack, I.H. Jung, Y.B. Kang, J. Melançon, FactSage thermochemical software and databases 2010–2016. *Calphad*. 2016; 35–53.
17. FactSage, Montreal, Canada. Available online: [www.factsage.com](http://www.factsage.com) (accessed on 20 December 2022)
18. S. Vyazovkin, A. K. Burnham, J. M. Criado, L. A. Pérez-Maqueda, C. Popescu, and N. Sbirrazzulli, *ICTAC Kinetics Committee recommendations for performing kinetic computations on thermal analysis data* *Thermochim Acta*. **520**, 2011 (1–19). <https://doi.org/10.1016/j.tca.2011.03.034>.
19. M. Vázquez, I. Moreno-Ventas, I. Raposo, A. Palma, and M. J. Díaz, *Journal of Thermal Analysis and Calorimetry*. **141**, (3), 2020 (1157–1163). <https://doi.org/10.1007/s10973-019-09098-4>.
20. S. Hasani, P. Rezaei-Shahreza, and A. Seifoddini, *Journal of Thermal Analysis and Calorimetry*. **143**, (5), 2020 (3365–3375). <https://doi.org/10.1007/s10973-020-09716-6>.
21. J. Yang, S. Liu, Q. Dai, Z. Guo, R. Ao, J. Pan, Y. Yang, Y. Yang, and L. Ma, *Fuel*. **306**, 2021 (121668). <https://doi.org/10.1016/j.fuel.2021.121668>.
22. H. L. Friedman, *Journal of Polymer Science Part C: Polymer Symposia*. **6**, (1), 1964 (183–195). <https://doi.org/10.1002/polc.5070060121>.
23. A. W. Coats and J. P. Redfern, *Nature*. **201**, (4914), 1964 (68–69). <https://doi.org/10.1038/201068a0>.
24. K. R. Ebrahimi and M. H. Abbasi, *Transactions of Nonferrous Metals Society of China*. **18**, (1), 2008 (217–221). [https://doi.org/10.1016/s1003-6326\(08\)60039-4](https://doi.org/10.1016/s1003-6326(08)60039-4).
25. H. E. Kissinger, *Analytical Chemistry*. **29**, (11), 1957 (1702–1706). <https://doi.org/10.1021/ac60131a045>.
26. T. Akaheira and T. Sunose, *Res Rep Chiba Inst Technol (Sci Technol)*. **16**, 1971 (22–31).
27. J. H. Flynn and L. A. Wall, *Journal of Research of the National Bureau of Standards Section A: Physics and Chemistry*. **70A**, (6), 1966 (487). <https://doi.org/10.6028/jres.070a.043>.
28. T. Ozawa, *Journal of Thermal Analysis*. **9**, (3), 1976 (369–373). <https://doi.org/10.1007/bf01909401>.
29. J. Li and J. Mayer, *Materials Chemistry and Physics*. **32**, (1), 1992 (1–24). [https://doi.org/10.1016/0254-0584\(92\)90243-2](https://doi.org/10.1016/0254-0584(92)90243-2).
30. F. Yi, J. B. DeLisio, N. Nguyen, M. R. Zachariah, and D. A. LaVan, *Chemical Physics Letters*. **689**, 2017 (26–29). <https://doi.org/10.1016/j.cplett.2017.09.066>.
31. R. Chen and S. A. A. Winer, *Journal of applied physics*. **41**, (13), 1970 (5227–5232). <https://doi.org/10.1063/1.1658652>.
32. P. Sánchez-Jiménez, J. Criado, and L. Pérez-Maqueda, *Journal of thermal analysis and calorimetry*. **94**, (2), 2008 (427–432). <https://doi.org/10.1007/s10973-008-9200-2>.
33. S. Vyazovkin, *Molecules*. **25**, (12), 2020 (2813). <https://doi.org/10.3390/molecules25122813>.
34. H. Jalkanen, *Scand. J. Metall.* **10**, (6), 1981 (257–326).

**Publisher's Note** Springer Nature remains neutral with regard to jurisdictional claims in published maps and institutional affiliations.



## Authors and Affiliations

**M. Vázquez Vázquez<sup>1,2</sup> · M. J. Díaz Blanco<sup>3,4</sup> · R. A. Parra Figueroa<sup>5</sup> ·  
E. R. Balladares Varela<sup>5</sup> · O. Jerez Riveros<sup>6</sup> · M. Cuevas Cerda<sup>5</sup> ·  
I. Moreno-Ventas Bravo<sup>1,7</sup>**

✉ M. J. Díaz Blanco  
dblanc@uhu.es

M. Vázquez Vázquez  
vazquez.marta1991@gmail.com

<sup>1</sup> Faculty of Experimental Science, University of Huelva, 21007 Huelva, Spain

<sup>2</sup> Atlantic Copper S.L.U., 21001 Huelva, Spain

<sup>3</sup> Higher Technical School of Engineering, University of Huelva, 21007 Huelva, Spain

<sup>4</sup> Centre for Research in Product Technology and Chemical Processes (Pro2TecS), University of Huelva, 21007 Huelva, Spain

<sup>5</sup> Metallurgical Engineering Department, University of Concepción, 4070386 Concepción, Chile

<sup>6</sup> Institute of Applied Economic Geology, University of Concepción, 4070386 Concepción, Chile

<sup>7</sup> Center for Research in Sustainable Chemistry (CIQSO), University of Huelva, 21007 Huelva, Spain